Supporting Material for: Solvent States and Spectroscopy of Doped Helium Clusters as a Quantum-Chemistry-like Problem†

Néstor F. Aguirre,[a] Pablo Villarreal,[a] Gerardo Delgado-Barrio,[a] Alexander Mitrushchenkov,[b] and María Pilar de Lara-Castells*[a]

[a] Instituto de Física Fundamental, CSIC, Serrano 123 28006 Madrid, Spain; Tel: 34-915616800; E-mail: Pilar.deLara.Castells@csic.es.
* Corresponding author, E-mail: Pilar.deLara.Castells@csic.es.
[b] Université Paris-Est, Laboratoire Modélisation et Simulation Multi Echelle, MSME UMR 8208 CNRS, 5 bd Descartes, 77454 Marne-la-Vallée, France.

1 Fitting of the He-$Cl_2(X)$ potential energy surface

The analytical functional form of the He-$Cl_2(X)$ potential energy surface (PES) was obtained by fitting the *ab initio* data provided by Cybulski and Holt [1] at six equidistant angular values θ_i. Briefly, we employed a Legendre polynomial expansion in θ and a fitting to Morse-var der Waals functions in R [2] with the Cl-Cl internuclear distance r fixed to its equilibrium value. This fitting procedure gives a relative error of $\sim 0.01\%$ around the global minimum, increasing up to $\sim 0.5\%$ at the repulsive regions. Explicitly, the Legendre polynomial expansion can be written as:

$$V'_{\mathrm{He-Cl_2}}(R,\theta;r_e) = \sum_{\lambda=0}^{5} V_\lambda(R;r_e) P_{2\lambda}(\cos\theta) \tag{1}$$

where the $V_\lambda(R;r_e)$ coefficients were obtained by applying the collocation method. Firstly, at each angular value θ_i $(i = 1-6)$, a Morse-van der Waals function

$$V'_{\mathrm{He-Cl_2}}(R,\theta_i;r_e) = D_i\left[e^{-2\alpha_i(R-R_{ei})} - 2e^{-\alpha_i(R-R_{ei})}\right] + \left(\frac{c_{8i}}{R}\right)^8 - \left(\frac{c_{6i}}{R}\right)^6 \tag{2}$$

was fitted to the *ab initio* data. The different parameters D_i, R_{ei}, c_{8i}, and c_{6i} were obtained using a nonlinear square fitting procedure. The resulting values are given in Table 1. Hereafter, the coefficients $V_\lambda(R;r_e)$ were obtained by solving Eq. 1. Explicitly,

$$V_\lambda(R;r_e) = \left\{\mathbf{P}(\boldsymbol{\theta})^{-1}\mathbf{V}'_{\mathrm{He-Cl_2}}(R,\boldsymbol{\theta};r_e)\right\}_\lambda \quad \lambda = \{0,1,\cdots,5\}. \tag{3}$$

The differences between the *ab initio* energies and those provided by the fitting procedure are displayed in Table 2.

2 Additional details of the FCI Nuclear Orbital calculations

The analytic potential derived by Aziz and Slaman [3] was employed to account for the He-He interaction. The helium dimer potential published very recently by Cenket et al. [4] is more accurate. It was obtained from very accurate BO calculations, that includes non-BO adiabatic and relativistic corrections as well as quantum electrodynamic effects. The differences between both He-He potentials (about 0.02 cm^{-1} at the minimun) influence very little the energies for cluster sizes in which the He-dopant interaction dominates. This is our case, with the He-Cl_2 potential wells being about six times deeper than the He-He potential well (about -7.6 cm^{-1}). Using both He-He potentials, the the ground-state energies of $(^3He)_N$-$Cl_2(X)$ clusters with $N = 3$ and 4 differ by 0.02 and 0.03 $cm,^{-1}$ respectively, below 0.05% of the total energies. Contrarily, the energy of the ^4He dimer bound state calculated with the potential by Aziz and Slaman is about 20% higher than the best estimate by Cenket et al. [4]. The FCI-NO energies of ground- and excited states (up to 40 states) were obtained by setting $l_{\max} = m_{\max} = 9$ (8) and $n = 4$ for ^4He (^3He), with up to 170 million of CSFs and 400 one-particle basis functions [5].

			$r = 1.99\,\mathring{A}$			
θ_i	D_i	α_i	R_{ei}	c_{6i}	c_{8i}	σ
deg.	cm^{-1}	$\mathring{A}^{-1}$	$\mathring{A}$	$\mathring{A}(cm^{-1})^{1/6}$	$\mathring{A}(cm^{-1})^{1/8}$	cm^{-1}
0°	131.3(68)	2.0436(83)	4.20(13)	10.04(36)	7.56(93)	0.093
20°	56.5(41)	1.9547(69)	4.45(20)	9.67(41)	6.6(23)	0.057
40°	39.9(34)	1.8539(95)	4.48(25)	9.54(34)	7.0(13)	0.020
60°	131.0(16)	1.817(30)	3.83(43)	9.58(41)	7.81(74)	0.034
80°	182.2(30)	1.881(47)	3.29(60)	9.24(27)	7.24(63)	0.023
90°	11.2(33)	1.821(27)	4.19(91)	8.77(21)	2.6(17)	0.079

Table 1: Fitted parameters for the analytical functional form of the He-$Cl_2(X)$ interaction potential. The *ab-initio* energies were taken from a previous work by Cybulski and Holt [1]. The standard errors are given in parenthesis, with the numbers corresponding to the last two digits of the value (i.e., $c_6 = 10.04 \pm 0.36$ $cm^{-1} = 10.04(36)$). Values corresponding to the standard deviation σ are also provided.

R/θ	0.0°	20.0°	40.0°	60.0°	80.0°	90.0°
2.75	-	-	-	-	-	4.77
3.00	-	-	-	-	3.41	0.01
3.25	-	-	-	3.56	0.01	−0.06
3.50	6.38	4.94	2.70	0.01	−0.03	0.08
3.75	0.00	0.00	0.00	−0.03	0.04	0.03
4.00	−0.02	−0.02	−0.01	0.04	0.00	−0.05
4.25	0.05	0.04	0.02	0.01	−0.03	−0.05
4.50	−0.03	−0.02	−0.01	−0.04	−0.01	−0.01
5.00	−0.04	−0.03	−0.02	−0.01	0.00	0.01
5.50	0.05	0.04	0.02	0.03	0.03	0.06
7.00	−0.03	−0.02	−0.01	0.00	0.00	0.02

Table 2: Energy differences (in cm^{-1}) between the *ab initio* data provided by Cybulski and Holt [1] and the values obtained after the fitting procedure at different R (in Å) and θ (in degrees) values.

3 Vibro-rotational Raman spectra within the linear rotor approximation for the diatomic dopant

The FCI-NO states were labeled following the conventional notation of electronic states for diatomic molecules, $n\,^{2S+1}\Lambda^{(\pm)}_{(g/u)}$, with Λ and S being, respectively, the projection of the total He orbital angular momenta $\mathbf{L} = \sum_N \mathbf{l}_k$ on the molecular axis, and the spin angular momentum quantum number. Within the linear rotor approximation for the diatomic dopant, the effective cluster Hamiltonian reads, $\hat{H}_{\rm eff} = \hat{H} + B_v\,\mathbf{j},^2$ with $\mathbf{j}$ and B_v being the diatomic rotational angular momentum and the rotational constant in the vibrational level $|v\rangle$, respectively. For a total angular momentum $\mathbf{J}$=$\mathbf{j}$+$\mathbf{L}$+$\mathbf{S}$ with a projection onto the body-fixed (BF) Z-axis $\Omega = \Lambda + \Sigma$ (Σ being the projection of $\mathbf{S}$ on Z), the vibro-rotational (Hund's case a) basis functions can be written as,

$$|I\rangle \equiv |J\ M; n\,^{2S+1}\Lambda^{(\pm)}_{(g,u)(\Omega)}\rangle_v = |v\rangle\ |n\,^{2S+1}\Lambda^{(\pm)}_{(g,u)}; \Lambda, \Sigma\rangle\ |J, \Omega, M\rangle$$

where $|J, \Omega, M\rangle$ are Wigner rotation matrices depending on the $\mathbf{r}$ polar components in the space-fixed (SF) frame. The diagonal matrix elements of the cluster Hamiltonian read,

$$\begin{aligned}\langle I|\hat{H}_{\rm eff}|I\rangle &= \epsilon_v + \mathcal{E}^{\rm FCI-NO}(n\,^{2S+1}\Lambda^{(\pm)}_{(g/u)}) \\ &+ B_v\left[\langle n\,^{2S+1}\Lambda^{(\pm)}_{(g/u)}|L^2_\perp|n\,^{2S+1}\Lambda^{(\pm)}_{(g/u)}\rangle - \Omega^2 - \Sigma^2 + S(S+1) + J(J+1)\right]\end{aligned} \tag{4}$$

where ϵ_v is the energy of the diatomic in the vibrational level $|v\rangle$ and $\langle L^2_\perp\rangle = \langle L^2_x + L^2_y\rangle$. Since $\mathbf{L}^2$ is a two-particle property (the orbital angular momenta of the helium atoms are coupled), a wave-function-based method is needed to obtain it, or at least, approaches capable of providing the second-order reduced density matrix. Explicitly,

$$\langle n\,^{2S+1}\Lambda^{(\pm)}_{(g/u)}|\mathbf{L}^2|n\,^{2S+1}\Lambda^{(\pm)}_{(g/u)}\rangle = \sum_{ijkl} L_{ij}L_{kl}\Gamma_{ij;kl} + \sum_{ij} L^2_{ij}\gamma_{ij},$$

with Γ and γ as the second- and first-order reduced density matrices in the chosen one-particle basis set, L_{ij} and L^2_{ij} being, respectively, the matrix representations of the total He angular momentum operator and its square on that basis.

The adopted treatment simplifies the adiabatic approach for the diatomic stretch mode. It is justified if the r-dependence of both FCI-NO energies and $\langle \mathbf{L}^2 \rangle$ expectation values are negligible as compared to that of the diatomic potential in the relevant range of internuclear distances for the considered vibrational transition. Otherwise, a modified dopant Schrödinger equation $\left(\hat{h}^{\rm eff} - \epsilon_{JS\Lambda\Sigma v}\right) |v\rangle_{JS\Lambda\Sigma}$ should be solved for the different FCI-NO states, and associated (Σ, Λ) pair of quantum numbers, at each J value [6, 7]

$$\hat{h}^{\rm eff} = -\frac{\hbar^2}{2m}\frac{\partial^2}{\partial r^2} + U(r) + \mathcal{E}^{\rm FCI-NO}(r) + \frac{\hbar^2}{2mr^2}\langle \mathbf{j}^2 \rangle \tag{5}$$

with m and $U(r)$ being the diatomic mass and the internuclear potential, respectively. For transitions between the lowest vibrational levels, the approximation can be considered as appropiate. For example, the depth of the molecular bromine potential is modified by only 1% due to the r-dependence of the ground-state energy corresponding to four helium atoms around the dopant.

The main approximations involved in the applied QC-like approach are therefore: (1) the pair-wise approach for the global potential energy surface; (2) the linear rotor approximation for the diatomic dopant; (3) the decoupling of the diatomic rotation from the He motion. The validity of the pair-wise approach has been assessed by *ab-initio* calculations on complexes with up to four ^{4}He atoms [8]. The approximation of decoupling the molecular rotation has also been tested for heavy as well as light host molecules and two ^{4}He atoms [9, 10]. As discussed below, the current version of the FCI-NO implementation allows to incorporate the Coriolis non-adiabatic couplings between ground and excited states.

The inclusion of Coriolis couplings makes the diatomic rotational term, $B_v\, \mathbf{j}^2 \equiv B_v\, [(\mathbf{J} - \mathbf{S}) - \mathbf{L}]^2$, no longer diagonal in the Hund's case a basis. Explicitly, using the auxiliary function,

$$f^{\pm}_{ab} = \sqrt{a(a+1) - b(b \pm 1)},$$

the off-diagonal Hamiltonian matrix elements between the vibro-(spin)rotational levels $|I\rangle$ and $|I'\rangle$ can be written as,

$$\langle I | B_v \left(L^+ S^- + L^- S^+\right) |I'\rangle = B_v\, f^{\pm}_{S_I \Sigma_I} \langle I | L^{\mp} | I' \rangle \tag{6}$$

if $\Delta\Lambda (\equiv \Lambda_{I'} - \Lambda_I) = -\Delta\Sigma = \pm 1$ and $\Delta S = \Delta\Omega = 0$.

$$\langle I | - B_v \left(J^+ L^- + L^- J^+\right) |I'\rangle = -B_v\, f^{\pm}_{J_I \Omega_I} \langle I | L^{\mp} | I' \rangle \tag{7}$$

if $\Delta\Lambda = \Delta\Omega = \pm 1$ and $\Delta\Sigma = \Delta S = 0$.

$$\langle I | - B_v \left(J^+ S^- + J^- S^+\right) |I'\rangle = -B_v\, f^{\pm}_{S_I \Sigma_I} f^{\pm}_{J_I \Omega_I} \tag{8}$$

if $\Delta\Sigma = \Delta\Omega = \pm 1$ and $\Delta\Lambda = \Delta S = 0$.

Further symmetry considerations allow to define parity-adapted basis functions. In the BF frame, for the Hund's case (a), the parity-adapted vibro-(spin)rotational basis can be expressed as [11],

$$\begin{aligned} |J\ M; n\ ^{2S+1}\Lambda^{(\pm)}_{(g,u)(p^{\pm},\Omega)}\rangle_v &= \frac{1}{\sqrt{2 - \delta_{\Lambda 0}\delta_{\Sigma 0}}}\, |v\rangle \times \\ \times \left(|n\ ^{2S+1}\Lambda^{(\pm)}_{(g,u)}; \Lambda, \Sigma\rangle |J, \Omega, M\rangle \pm |n\ ^{2S+1}\Lambda^{(\pm)}_{(g,u)}; -\Lambda, -\Sigma\rangle\ |J, -\Omega, M\rangle\right), \end{aligned}$$

where the $p^{\pm}$ blocks have parity $\pm(-1)^{J-S+\sigma}$, with $\sigma = 1$ for Σ^- helium states and $\sigma = 0$ otherwise.

3.1 Spectral line positions and intensities.

The incident ligth is assumed to be linearly polarized and propagating along the space-fixed (SF) y' axis, with the scattered ligth detected along the SF x' axis. A Boltzmann distribution of the solvent states at a given temperature is assumed within the chosen temperature range $[0.07 - 1.0$ K$]$. The expression for the intensity of the spectral lines is (see also the main text),

$$I_{fi}(T) \propto \frac{e^{-(\varepsilon_i/kT)}}{\sum_i e^{-(\varepsilon_i/kT)}}\, \frac{1}{2J_i + 1} \sum_{M_i} |\langle f | \mu_0 | i \rangle|^2 \tag{9}$$

where i (f) is a collective index denoting the quantum numbers of the initial (final) state. The transition induced dipole matrix elements $\langle f|\mu_0|i\rangle$ can be expressed in terms of the spherical $\alpha_{f,i}$ and the anisotropic $\beta_{f,i}$ polarizability components of the diatomic [12] as,

$$\langle f|\mu_0|i\rangle = \sum_{\Omega} c_{\Omega}^{(i)} c_{\Omega}^{(f)} \sqrt{(2J_i+1)(2J_f+1)} \;\times$$
$$\times \left[\alpha_{f,i} \begin{pmatrix} J_i & 0 & J_f \\ -M_i & 0 & M_i \end{pmatrix} \begin{pmatrix} J_i & 0 & J_f \\ -\Omega & 0 & \Omega \end{pmatrix} \right.$$
$$\left. + \frac{2\beta_{f,i}}{3} \begin{pmatrix} J_i & 2 & J_f \\ -M_i & 0 & M_i \end{pmatrix} \begin{pmatrix} J_i & 2 & J_f \\ -\Omega & 0 & \Omega \end{pmatrix}\right],$$

where $c_{\Omega}^{(i)}$ and $c_{\Omega}^{(f)}$ are the weights of a given Ω value in the initial and final states. According to the adopted definition for the intensity, it can be demonstrated that for $\Delta J = 0$ and integer J values, only transitions between spin-rotational states with the same parity ($p^{\pm} \rightarrow p^{\pm}$) are allowed while the opposite holds true for half-integer J values.

3.2 Broadening of the spectral lines: Vibrational Predissociation

In order to account for the broadening of the spectral lines, the same approach as in Ref. 2 was adopted. Between the relaxation processes that can contribute to the broadening, we consider the mechanism of vibrational predissociation (VP). Once the dopant molecule has reached the vibrational excited state, as a consequence of its interaction with the radiation, the energy excess can flow from the dopant to some of the weak He-dopant bonds causing its breaking. Schematically,

$$^{3,4}\mathrm{He@Cl_2}(X,\nu_i,n_i) + \hbar\omega \longrightarrow {}^{3,4}\mathrm{He@Cl_2}(X,\nu_f,n_f) \longrightarrow {}^{3,4}\mathrm{He}(\mathcal{E}) + \mathrm{Cl_2}(X,\nu). \qquad (10)$$

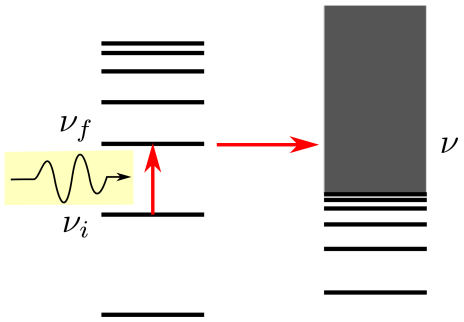

Within the framework of the adiabatic angular approach proposed by Beswick and Delgado-Barrio [13], the θ-dependent VP widths for the $^{3,4}\mathrm{He@Cl_2}(X,\nu_f,n_f)$ triatomic species are first estimated, $^{3,4}\Gamma_{\nu\leftarrow\nu_f}(\theta)$. To this end, we used the the (analytical) three-dimensional (3D) He-Cl_2 PES reported by Takayanagi et al. [14] (see Fig. 1). We notice that 3D PESs depending on the dopant internuclear distance (r) are necessary to carry out the VP calculations. On the other hand, the fitting procedure described in the previous section provides a two-dimensional analytical functional form of the PES upon fixing r to the equilibrium value ($r = r_e$). This is the reason why we used the 3D PES to account for the VP mechanism. Our fitting procedure provides smaller relative errors with respect to the *ab initio* data [1] at $r = r_e$. When different r values were considered, however, the r-dependence of the 3D PES was better represented by the analytical functional form reported by Takayanagi et al. [14].

The calculated VP widths are represented in Fig. 1. As apparent from the right-hand panel of this figure, the maxima of the θ-dependent VP widths correspond to the He-$Cl_2(X)$ complex at a linear configuration. In fact, the vibrational couplings exhibit a markedly orientational dependence, with the main contribution coming from nearly collinear configurations. In its turn, this is due to the stronger r-dependence of the PES at $\theta = 0°$. This has been found for other weakly bound complexes using an *ab initio* PES to characterize the interaction [15]. As the next step, the angular distributions $^{3,4}\mathcal{D}_{T,L}(\theta)$ of a helium atom around the dopant are calculated for the lowest-energy states with the density either at a T-shaped arrangement (T) or at the ends of the dopant (L). The energies of these

single-particle states are tabulated in Table 3 (the 1 σ_g and 2 σ_g orbitals). An average of the triatomic VP width is then obtained for both orbitals and helium isotopes. In the present case,

$$ {}^{3,4}\Gamma^{T,L}_{0\leftarrow 1} = \int_0^{\pi} {}^{3,4}\mathcal{D}_{T,L}(\theta)\, {}^{3,4}\Gamma_{0\leftarrow 1}(\theta)\, d\theta \tag{11} $$

The numerical values of the VP widths for the ^{4}He-$Cl_2(X)$ complex are,

$$ {}^4\Gamma^{T}_{0\leftarrow 1} = 1.73\cdot 10^{-6}\,\mathrm{cm}^{-1} \qquad {}^4\Gamma^{L}_{0\leftarrow 1} = 2.58\cdot 10^{-4}\,\mathrm{cm}^{-1} \tag{12} $$

and for the ^{3}He-$Cl_2(X)$ complex,

$$ {}^3\Gamma^{T}_{0\leftarrow 1} = 4.56\cdot 10^{-6}\,\mathrm{cm}^{-1} \qquad {}^3\Gamma^{L}_{0\leftarrow 1} = 2.87\cdot 10^{-4}\,\mathrm{cm}^{-1} \tag{13} $$

An estimation of the VP width associated to the N-sized complex at each final state (f) is obtained as the mean value,

$$ {}^{3,4}\Gamma^{(N)}_{(f)} \approx N_r\, {}^{3,4}\Gamma^{T}_{0\leftarrow 1} + \left(N - N_r\right) {}^{3,4}\Gamma^{L}_{0\leftarrow 1} \tag{14} $$

where N_r is the approximate number of helium atoms on the equatorial belt around the dopant for the complex [5]. Finally, by dressing with Lorentzian functions the stick lines of different intensities (see the main text), and summing over all transitions, a continuum profile for the vibro-rotational Raman signal is obtained:

$$ \sigma_N(\omega;T) = \frac{1}{2\pi}\sum_{f,i} \frac{\Gamma^{(N)}_{(f)}}{\hbar^2(\omega-\omega_{fi})^2 + \left(\Gamma^{(N)}_{(f)}/2\right)^2} I_{fi}(T). \tag{15} $$

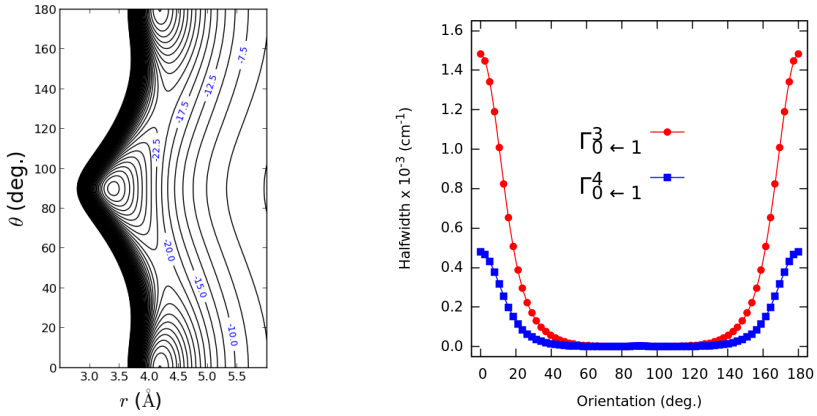

Figure 1: Left Panel: Contour plot of the He-$Cl_2(X)$ PES from Takayanagi et al. [14] as a function of the distance of the He atom from the Cl_2 center of mass (R) and θ, with the Cl-Cl internuclear distance r fixed to its equilibrium value ($r = 1.99$ Å). Right Panel: Calculated θ-dependent VP widths for the ^{3,4}He–$Cl_2(X, v_f)$ triatomic, using the PES represented at the left-hand panel.

4 Isotope and Cluster Size Dependence of the Dopant Vibro-rotational Raman Spectra: Additional details

Values for the total angular momentum $J \leq 10$ were included in the spectra simulations to achieve convergence at the chosen temperature range $[0.07 - 1.0$ K$]$. The $Cl_2(X)$ interaction was characterized by a Morse function [16]. Using this potential, values of 0.240 and 0.239 cm^{-1} were obtained for the diatomic rotational constant B_v in the vibrational states $v = 0$ and 1. The necessary polarizabilities of the dopant, assumed to be unchanged by complexation, were taken from the work carried out by

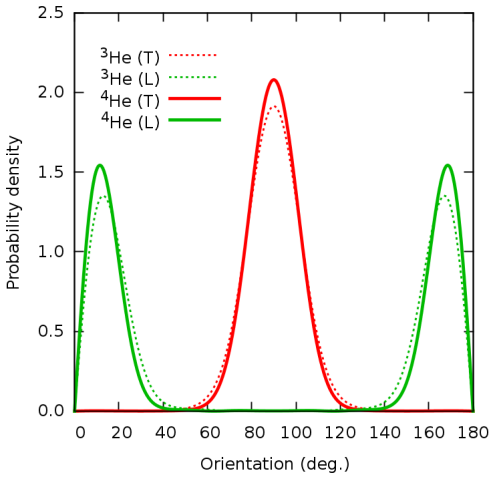

Figure 2: Angular distributions for the two lowest-energy states of the ^{3,4}He-$Cl_2(X)$ complex with the density at T-shapes and collinear configurations.

Maroulis [17]. As mentioned in the previous section, the angular dependent VP rates for the (^{3,4}He)-Cl_2 (X) complex were obtained by using the three-dimensional *ab initio* He-dopant potential from [14]. The calculated spectra (see Figs. 3 and 4 as well as Fig. 8 of the main text), display continuum profiles of the scattered photon intensity as a function of the energy loss between the incident and the exiting photons, $\hbar w_0$ - $\hbar w_{fi}$. These energies are given relative to the bare dopant transition (J,v)=(0,1) ← (0,0), 554.37 cm.$^{-1}$

4.1 Coriolis coupling effects in the vibro-rotational spectra of the (^{4}He)$_3$-Cl_2 cluster

The left panel of Fig. 3 shows the low-resolution spectra of the (^{4}He)$_3$-Cl_2 cluster as well as an enlarged view of the more intense Q-branch ($\Delta J = 0$). The right-hand panel of this figure, depicts the spin-rotational levels obtained without including the Coriolis couplings (highlighted in red), and adding them (highlighted in black), as well as the correlation between both sets of energy levels.

For spinless ^{4}He atoms ($S = 0$), the only possible Coriolis term stem from the $-B_v(J^+L^- + L^-J^+)$ operator, (referred to as the L-decoupling operator), causing the mixing between states that differ by $\Delta\Lambda = \pm 1$. We can notice in Fig. 3 that the energy and relative positions of the rotational levels are almost unperturbed by these couplings. Thus, the mixing percentage is smaller than 4% at $J \leq 10$. As can be seen in Table 8 from the supplementary material†, the expectation values $\langle L^\pm \rangle$ are with only one exception, below 0.1. As already mentioned in [5] for $N = 4$, the largest values ($\langle L^\pm \rangle \geq$ 0.05 a.u.) involve the exchange of one helium atom between the equatorial ring and the dopant poles. Due to the Σ symmetry of the ground-state for the bosonic wave-function, the excited states with Π symmetry are the most relevant when the Coriolis couplings are accounted for. As discussed in the section 3 of the main text, these excited states are damped down due to the high frequencies of the implied stretching He-He modes when the symmetric condition for the spinless wave-function is imposed (see Fig. 6 of the main text). The small value of the dopant rotational constant ($\sim$ 0.24 cm^{-1}), also contributes to render the global value from the Coriolis term $-B_v(J^+L^- + L^-J^+)$ very small. As a result, the dopant spectra in ^{4}He is unperturbed by the inclusion of Coriolis couplings, indicating the adiabatic following of the dopant rotation by the ^{4}He atoms. The left panel of Fig. 3 shows the low-resolution spectra as well as an enlarged view of the more intense Q-branch ($\Delta J = 0$). It can be observed that excited states implying the vibrational He-He motion (Π states) contribute very little to the spectra. Similar considerations apply to excited states involving the bending He-dopant vibrational mode (states with $N_r \leq 3$). Still, a rotational band from the $2\ ^1_2\Sigma^+_u$ state can be identified in the Q-branch (see Fig. 3). Notice that the broadening of the stick line associated to the $2\ ^1_2\Sigma^+_u$ state is larger. In fact, the VP process is much faster for helium atoms located in a collinear configuration, as earlier found for other weakly bound complexes using an *ab initio* PES with minima

located at both T-shaped and collinear arrangements [15]. This results in the enhanced broadening of stick lines corresponding to transitions between states having helium density along the molecular axis such as the $2\ ^1_2\Sigma^+_u$ state. Among the excited states, the collective rotational $1\ ^1_3\Phi_u$ state contributes the most to the spectra, with relatively high intensity peaks at both Q- and R-branch regions with $J = \Lambda = 3$.

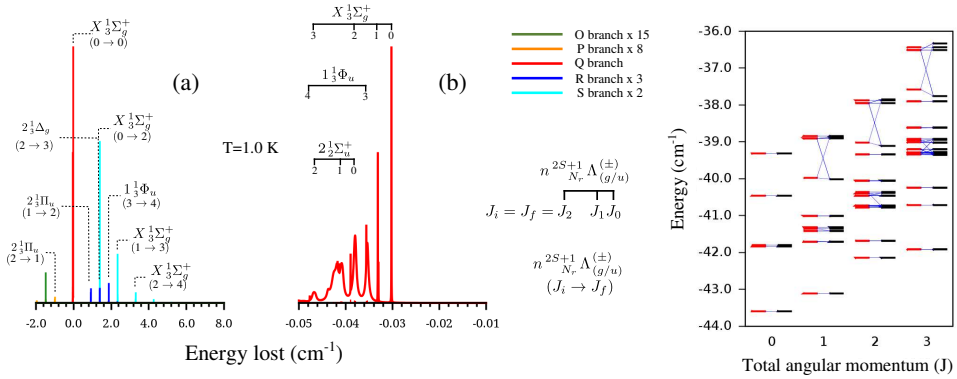

Figure 3: Left panel: Vibro-rotational Raman ($v = 1 \leftarrow 0$) spectra of the $(^4\text{He})_3$-$Cl_2(X)$ cluster (perturbed Cl_2) at $T = 1.0$ K. An enlarged view of the (main) Q-branch region ($b = a \times 125$) is shown at the right-hand side. Right panel: Graphical representation of spin-rotational energy levels of $^4\text{He}_3$-$Cl_2(X)$ as a function of the total angular momentum quantum number J, without including Coriolis couplings (highlighted with red lines) and including them (depicted with black lines). Blue lines have been drawn to follow the correlation between both sets of spin-rotational levels, with the coefficients combining them larger than $10.^{-4}$

4.2 Coriolis coupling effects in the vibro-rotational spectra of the $(^3\text{He})_3$-Cl_2 cluster

In Figure 4, the vibro-rotational Raman spectra of the $(^3\text{He})_3$-Cl_2 cluster with and without adding Coriolis couplings are compared. Without including Coriolis couplings, the spectrum is clearly dominated by contributions from spin-rotational levels with $J = 1/2$, as expected. When the Coriolis effects are included, however, additional branches from spin-rotational levels with $J = 3/2$ do appear. Additionally, the most intense Q-type peak arises from the ground-state of Σ-symmetry when adding the Coriolis terms, replacing the lowest-energy Π-symmetry state as the most contributing state. At $T = 1$ K, both Σ and Π-symmetry states cooperate to provide a congested spectrum in which several Q-type peaks are coexisting. Contrarily, the spectrum without adding Coriolis term holds an unique high-intensity Q-type peak. Between the different Coriolis operators acting on fermionic states, the spin-decoupling operator $-B_v(J^+S^- + J^-S^+)$ plays the major role. Still, the influence of the L-decoupling operator $-B_v(J^+L^- + J^-L^+)$ is not negligible and much more pronounced than for the ^{4}He isotope. Similarly to the case with $N = 4$ [5] the mixing percentage between Σ and Π-symmetry states induced by the L-decoupling operator is one order of magnitude larger than in ^{4}He. Specifically, it is about 3.6%, 4.2% and 24.6% for $J = 1/2$, $3/2$ and $7/2$. No significant differences are found for the $\langle \Lambda \pm 1|L^{\pm}|\Lambda\rangle$ values obtained for the ^{4}He and ^{3}He isotopes (see Table 8). In fact, the main reason for the larger mixing in ^{3}He is the much lower excitation energy of the Π-symmetry state when compared with the ^{4}He counterpart. In its turn, this is due to the key role of the spin degree of freedom in making the wave-function antisymmetric, rendering purely rotational states at any Λ value possible (without implying the He-He stretching modes). The energies of these states is about $B^{||}_{\text{eff}}/N_r \times \Lambda^2$ or even lower due to additional correlation effects. The two-fold degeneracy of Π-symmetry states also cooperates to make the Boltzmann factors larger, raising their peak intensities [5].

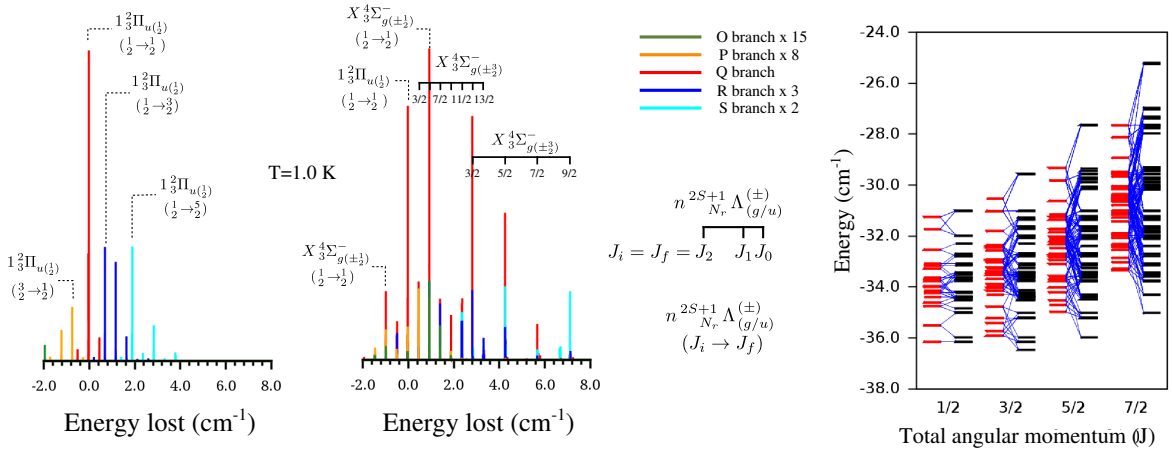

Figure 4: (color online) Left panel: Vibro-rotational Raman ($v = 1 \leftarrow 0$) spectra of the $(^4\text{He})_3$-$\text{Cl}_2(X)$ cluster (perturbed Cl_2) at $T = 1.0$ K. Left-side (a): Spectra without adding Coriolis couplings. Right-side (b): Spectra obtained after adding Coriolis couplings. Right panel: Graphical representation of spin-rotational energy levels of $^3\text{He}_3$-$\text{Cl}_2(X)$ as a function of the total angular momentum quantum number J, without including Coriolis couplings (highlighted with red lines) and including them (depicted with black lines). Blue lines have been drawn to follow the correlation between both sets of spin-rotational levels, with the coefficients combining them larger than $10.^{-4}$

5 Effective renormalization of the diatomic rotational constant including Coriolis couplings

As mentioned in the main text, an effective renormalization of the rotational constant including Coriolis couplings can be simply estimated. The three panels of Fig. 5 show the energies of the vibro-rotational energy levels arising from different FCI-NO states, as a function of $J(J+1)$ for $(^3\text{He})_N$-$\text{Cl}_2(X)$ clusters ($N = 2$ and 4), with the diatomic in the ground vibrational state ($v = 0$). As can be noticed from Fig. 5, the action of the $\mathbf{J} \cdot \mathbf{S}$ Coriolis operator gives rise to different vibro-rotational states as far as $S \neq 0$, showing the increase of the energy splitting with the value of $J(J+1)$. For example, as can be seen in the middle panel of Fig. 5, the quintet $1\,^5\Sigma_u^-$ state splits into five vibro-(spin)rotational levels with different J-dependent energies (distinct levels are represented with different colors in the figure). On the other hand, the triplet $X\,^3\Sigma_g^-$ state splits into three different vibro-rotational energy levels. As a result, the positions of the spectral lines stemming from those states as a function of J (see Fig. 6) exhibit turnaround points from which the J-dependent shift lies in the opposite direction.

Within the linear rotor approximation adopted in this work, the energies of the vibro-rotational levels arising from the singlet $^1\Sigma_g^+$ state exhibit a linear dependence on $J(J+1)$, with the slope equal to the rotational constant B_v (i.e., it is unaffected by the $\mathbf{J} \cdot \mathbf{S}$ operator). Naturally, the same holds true for the vibro-rotational energy levels of spin-less $(^4\text{He})_N$-$\text{Cl}_2(X)$ clusters. Thus, with rotational assignments of the spectra, the rotational constants can be derived by fitting the line positions to:

$$\hbar\omega_{fi} = \hbar\omega_0 + B_{v=1} J_f(J_f+1) - B_{v=0} J_i(J_i+1) \tag{16}$$

where $\hbar\omega_0$ is the band origin.

Due to the action of the $\mathbf{J} \cdot \mathbf{S}$ operator, however, the energy dependence of the vibro-(spin)rotational energy levels departs from this simple linear behaviour for $(^4\text{He})_N$-$\text{Cl}_2(X)$ clusters with $S \neq 0$. Still, it is possible to estimate an effective rotational constant from the quasi-linear dependence at larger values of $J(J+1)$ (see Fig. 6). By fitting the energy values corresponding to the lowest-energy vibro-(spin) rotational energy levels (highlighted with red bullets), effective renormalization of the rotational constants by $0.43B_v$ and $0.72B_v$ can be derived for the $1\,^5\Sigma_u^-$ and $X\,^3\Sigma_g^-$ FCI-NO states, respectively. Therefore, as can be expected, the Coriolis couplings effectively reduce the value of this constant. The inclusion of the lowest-energy vibro-(spin)rotational energy levels only can be considered as equiva-

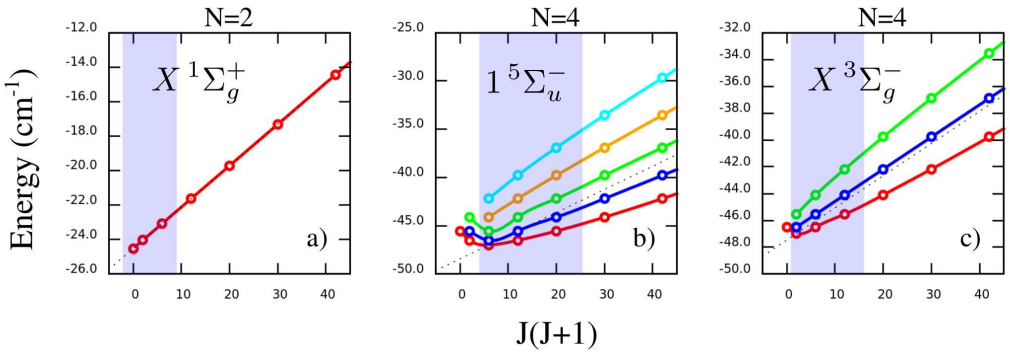

Figure 5: Energies of vibro-rotational energy levels as a function of $J(J+1)$, with J as the total angular momentum quantum number. Left-hand panel: $(^3\mathrm{He})_2$-$\mathrm{Cl}_2(X)$ cluster in the FCI-NO $X\ ^1\Sigma_g^+$ state. Middle panel: $(^3\mathrm{He})_4$-$\mathrm{Cl}_2(X)$ cluster in the maximum spin FCI-NO $1\ ^5\Sigma_u^-$ state. Right-hand panel: $(^3\mathrm{He})_4$-$\mathrm{Cl}_2(X)$ cluster in the (lowest-energy) FCI-NO $X\ ^3\Sigma_g^-$ state. Blue shaded areas correspond to the energy levels contributing to the two highest-intensity peaks within the O, P, Q, R, and S branches of the vibro-rotational Raman spectra at $T \leq 1$ K, with the red line correlating with the initial (lowest-energy) levels.

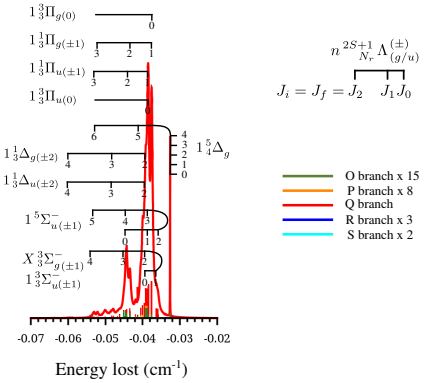

Figure 6: Rotational assignments ($J_i = J_f$) of the spectral lines positions at the (main) Q-branch region for the vibro-rotational Raman ($v = 1 \leftarrow 0$) spectra of $(^3\mathrm{He})_4$-$\mathrm{Cl}_2(X)$ at $T = 1$ K.

lent to derive an effective B_v value from the assignments of the line positions corresponding to the highest-intensity spectral peaks.

References

[1] S. M. Cybulski and J. S. Holt, J. Chem. Phys. **110**, 7745 (1999).

[2] A. Valdés, R. Prosmiti, P. Villarreal, G. Delgado-Barrio, and H.-J. Werner, J. Chem. Phys. **126**, 204301 (2007).

[3] R. A. Aziz and M. J. Slaman, J. Chem. Phys. **94**, 8047 (1991).

[4] W. Cencek, M. Przybytek, J. Komasa, J. B. Mehl, B. Jeziorski, and K. Szalewicz, J. Chem. Phys. **136**, 224303 (2012).

[5] N. F. Aguirre, P. Villarreal, G. Delgado-Barrio, A. O. Mitrushchenkov, and M. P. de Lara-Castells, Chem. Phys. Lett. **555**, 12 (2013).

[6] D. López-Durán, M. P. de Lara-Castells, G. Delgado-Barrio, P. Villarreal, C. Di Paola, F. A. Gianturco, and J. Jellinek, Phys. Rev. Lett. **93**, 053401 (2004).

[7] D. López-Durán, M. P. de Lara-Castells, G. Delgado-Barrio, P. Villarreal, C. Di Paola, F. A. Gianturco, and J. Jellinek, J. Chem. Phys. **121**, 2975 (2004).

[8] A. Valdés, R. Prosmiti, P. Villarreal, and G. Delgado-Barrio, J. Phys. Chem. A **116**, 7169 (2012).

[9] O. Roncero, R. Pérez-Tudela, M. P. de Lara-Castells, R. Prosmiti, G. Delgado-Barrio, and P. Villarreal, Int. J. Quantum Chem. **107**, 2756 (2007).

[10] O. Roncero, M. P. de Lara-Castells, G. Delgado-Barrio, P. Villarreal, T. Stoecklin, A. Voronin, and J. C. Rayez, J. Chem. Phys. **128**, 164313 (2008).

[11] R. Zare, *Angular Momentum*, Wiley, New York, 1988.

[12] E. B. Wilson, Jr., J. C. Decius, and P. C. Cross, *Molecular Vibrations: The Theory of Infrared and Raman Vibrational Spectra*, McGraw-Hill Book Company, Inc. (Reprinted by Dover Publications in 1980), New York, 1955.

[13] J. A. Beswick and G. Delgado-Barrio, J. Chem. Phys. **73**, 3653 (1980).

[14] T. Takayanagi, M. Shiga, and T. Taketsugu, J. Theor. Comp. Chem. **4**, 197 (2005).

[15] M. P. de Lara, P. Villarreal, G. Delgado-Barrio, S. Miret-Artés, E. Buonomo, and F. A. Gianturco, Chem. Phys. Lett. **242**, 336 (1995).

[16] K. P. Huber and G. Herzberg, *Molecular Spectra Molecular Structure, Constants of Diatomic Molecules*, Van Nostrand Reinhold, New York, 1979.

[17] G. Maroulis, Mol. Phys. **77**, 1085 (1992).

6 Energies, $\langle L^2 \rangle$ values, and Coriolis couplings of FCI-NO states

S	A_g	B_{3u}/B_{2u}	B_{1g}	B_{1u}	B_{2g}/B_{3g}	A_u
	^{4}He@Cl$_2$(X)					
0	-16.16 $1\sigma_g$	-16.08 $1\pi_u$	-14.86 $1\delta_g$	$-\underline{15.21}$ $1\sigma_u$	$-\underbrace{9.65}$ $1\pi_g$	$-\underbrace{7.59}$ $1\delta_u$
	6.78	7.40	6.80	13.20	13.22	10.37
	$-\underline{15.13}$ $2\sigma_g$	-13.54 $1\phi_u$	-11.01 $1\gamma_g$			
	12.74	7.44	6.85			
	^{3}He@Cl$_2$(X)					
1/2	-13.67 $1\sigma_g$	-12.98 $1\pi_u$	-12.06 $1\delta_g$	$-\underline{12.27}$ $1\sigma_u$	$-\underbrace{7.38}$ $1\pi_g$	$-\underbrace{5.19}$ $1\delta_u$
	5.52	5.06	5.67	9.57	8.39	8.82
	$-\underline{12.33}$ $2\sigma_g$	-9.76 $1\phi_u$	-7.35 $1\gamma_g$			
	10.14	5.28	6.85			

Table 3: Energies (in cm,$^{-1}$ first entry) and average values $\langle L_\perp^2 \rangle = \langle L_x^2 + L_y^2 \rangle$ (a.u., second entry) of ground and excited states of (^{3,4}He)-Cl$_2$(X) clusters (i.e., the independent-particle orbitals in FCI-NO calculations). The states are classified according to the symmetry within the D$_{2h}$ point group and the total spin quantum number, S. Underlined values are associated to states posing one helium atoms at the two Cl$_2$ ends. Values underlined with braces correspond to states having the helium density located at the two lateral rings around the dopant (see also Ref. 7).

S	A_g	B_{3u}/B_{2u}	B_{1g}	B_{1u}	B_{2g}/B_{3g}	A_u
	^{4}He$_2$@Cl$_2$(X)					
0	-32.42 $X\,{}^1_2\Sigma_g^+$	-32.00 $1\,{}^1_2\Pi_u$	-32.03 $1\,{}^1_2\Delta_g$	$-\underline{31.63}$ $1\,{}^1_1\Sigma_u^+$	$-\underline{31.55}$ $1\,{}^1_1\Pi_g$	$-\underline{30.33}$ $1\,{}^1_1\Delta_u$
	13.78	14.14	14.52	19.74	20.35	19.78
	$-\underline{31.56}$ $2\,{}^1_1\Sigma_g^+$	$-\underline{31.48}$ $2\,{}^1_1\Pi_u$	$-\underline{30.26}$ $1\,{}^1_1\Phi_g$	$-\underline{30.33}$ $1\,{}^1_1\Delta_u$		
	19.30	19.92	19.29	19.77		
	-31.11 $3\,{}^1_2\Sigma_g^+$	-30.66 $1\,{}^1_2\Phi_u$				
	13.82	14.17				
	-30.50 $2\,{}^1_2\Delta_g$					
	14.14					
	^{3}He$_2$@Cl$_2$(X)					
0	-27.09 $X\,{}^1_2\Sigma_g^+$	-26.15 $1\,{}^1_2\Pi_u$	-25.98 $1\,{}^1_2\Delta_g$	$-\underline{26.18}$ $1\,{}^1_1\Sigma_u^+$	$-\underline{25.49}$ $1\,{}^1_1\Pi_g$	$-\underline{24.58}$ $1\,{}^1_1\Delta_u$
	10.71	10.51	10.35	15.02	14.55	15.13
	$-\underline{26.24}$ $2\,{}^1_1\Sigma_g^+$					
	15.59					
1	$-\underline{26.24}$ $1\,{}^3_1\Sigma_g^+$	-26.73 $1\,{}^3_2\Pi_u$	-26.14 $1\,{}^3_2\Sigma_g^-$	$-\underline{26.18}$ $1\,{}^3_1\Sigma_u^+$	$-\underline{25.49}$ $1\,{}^3_1\Pi_g$	$-\underline{24.57}$ $1\,{}^3_1\Delta_u$
	15.55	10.49	10.11	14.99	14.46	15.14
		$-\underline{25.55}$ $2\,{}^3_1\Pi_u$				
		13.83				

Table 4: Energies (in cm,$^{-1}$ first entry) and average values $\langle L_\perp^2 \rangle = \langle L_x^2 + L_y^2 \rangle$ (a.u., second entry) of FCI-NO states for (^{3,4}He)$_2$-Cl$_2$(X) clusters. The FCI-NO states are classified according to the symmetry within the D$_{2h}$ point group and the total spin quantum number, S. Underlined (underlined with braces) values are associated to states posing about one helium atom at the two Cl$_2$ ends.

S	A_g	B_{3u}/B_{2u}	B_{1g}	B_{1u}	B_{2g}/B_{3g}	A_u
	^{4}He$_3$@Cl$_2(X)$					
0	$\underline{-48.58}$ $\underline{20.78}$ $\mathbf{X\,1^1_3\Sigma^+_g}$	$\underline{-47.76}$ $\underline{21.32}$ $1\,^1_3\Phi_u$	$\underline{-47.69}$ $\underline{26.76}$ $1\,^1_2\Delta_g$	$\underline{-48.13}$ $\underline{26.22}$ $1\,^1_2\Sigma^+_u$	$\underline{-47.72}$ $\underline{26.94}$ $1\,^1_2\Pi_g$	$\underline{-47.75}$ $\underline{27.26}$ $1\,^1_2\Delta_u$
	$\underline{-48.06}$ $\underline{26.07}$ $2\,^1_2\Sigma^+_g$	$\underline{-47.68}$ $\underline{25.09}$ $1\,^1_2\Pi_u$	-47.13 20.69 $2\,^1_3\Delta_g$	$\underline{-47.75}$ $\underline{27.27}$ $1\,^1_2\Delta_u$	$\underline{-46.39}$ $\underline{26.93}$ $1\,^1_2\Phi_g$	$\underline{-46.99}$ $\underline{26.87}$ $2\,^1_2\Delta_u$
	$\underline{-47.69}$ $\underline{26.77}$ $1\,^1_2\Delta_g$	-47.58 22.47 $2\,^1_3\Pi_u$	$\underline{-46.15}$ $\underline{26.36}$ $3\,^1_2\Delta_g$	$\underline{-46.84}$ $\underline{26.58}$ $2\,^1_2\Sigma^+_u$		
	$\underbrace{-46.98}$ 31.91 $3\,^1_1\Sigma^+_g$	$\underbrace{-46.92}$ 32.62 $3\,^1_1\Pi_u$				
		$\underline{-46.32}$ $\underline{26.47}$ $2\,^1_2\Phi_u$				
	^{3}He$_3$@Cl$_2(X)$					
1/2	$\underline{-39.90}$ $\underline{21.03}$ $1\,^2_2\Sigma^+_g$	-39.90 14.63 $1\,^2_3\Pi_u$	-39.46 15.70 $1\,^2_3\Delta_g$	$\underline{-39.83}$ $\underline{20.10}$ $1\,^2_2\Sigma^+_u$	$\underline{-39.46}$ $\underline{20.85}$ $1\,^2_2\Pi_g$	$\underline{-38.88}$ $\underline{19.48}$ $1\,^2_2\Sigma^-_u$
	-39.46 15.70 $1\,^2_3\Delta_g$	$\underline{-39.53}$ 20.39 $2\,^2_2\Pi_u$	$\underline{-38.96}$ 19.66 $1\,^2_2\Sigma^-_g$	$\underbrace{-38.73}$ 24.79 $2\,^2_1\Sigma^+_u$	$\underline{-38.89}$ 20.87 $2\,^2_2\Pi_g$	
3/2	$\underline{-38.61}$ $\underline{21.03}$ $2\,^4_2\Delta_g$	$\underline{-39.53}$ $\underline{20.41}$ $1\,^4_2\Pi_u$	-39.93 14.45 $\mathbf{X\,3^4_3\Sigma^-_g}$	$\underline{-38.54}$ $\underline{20.46}$ $1\,^4_2\Delta_u$	$\underline{-39.47}$ $\underline{19.78}$ $1\,^4_2\Pi_g$	$\underline{-38.88}$ $\underline{19.35}$ $1\,^4_2\Sigma^-_u$
	-37.95 15.37 $3\,^4_3\Delta_g$	-38.86 15.96 $1\,^4_3\Phi_u$	$\underline{-38.94}$ 20.05 $2\,^4_2\Sigma^-_g$		$\underbrace{-38.03}$ 24.21 $2\,^4_1\Pi_g$	
	-36.00 15.39 $1\,^4_3\Gamma_g$	-38.57 15.76 $2\,^4_3\Pi_u$	$\underline{-38.61}$ $\underline{21.03}$ $2\,^4_2\Delta_g$			
	$\underline{-35.53}$ $\underline{20.39}$ $2\,^4_2\Gamma_g$	$\underline{-37.89}$ $\underline{20.60}$ $2\,^4_2\Phi_u$	-37.95 15.37 $3\,^4_3\Delta_g$			

Table 5: Energies (in cm,$^{-1}$ first entry) and average values $\langle L^2_\perp\rangle = \langle L^2_x + L^2_y\rangle$ (a.u., second entry) of FCI-NO states for $(^{3,4}\mathrm{He})_3$-$\mathrm{Cl}_2(X)$ clusters. The FCI-NO states are classified according to the symmetry within the D_{2h} point group and the total spin quantum number, S. Underlined (underlined with braces) values are associated to states posing about two (one) helium atoms at the two Cl_2 ends.

S	A_g	B_{3u}/B_{2u}	B_{1g}	B_{1u}	B_{2g}/B_{3g}	A_u
	$^4He_4@Cl_2(X)$					
0	$\underline{-64.49}$ $\mathbf{X\,1^1_3\Sigma^+_g}$	$\underline{-63.66}$ $1\,^1_3\Phi_u$	-62.76 $1\,^1_4\Gamma_g$	$\underline{-64.55}$ $1\,^1_3\Sigma^+_u$	$\underline{-63.73}$ $1\,^1_3\Phi_g$	$\underline{-63.11}$ $1\,^1_3\Delta_u$
	-64.16 $2\,^1_4\Sigma^+_g$	$\underbrace{-63.34}$ $1\,^1_2\Pi_u$		-63.11 $1\,^1_3\Delta_u$	-63.58 $1\,^1_3\Pi_g$	
	$^3He_4@Cl_2(X)$					
0	$\underbrace{-52.60}$ $1\,^1_2\Sigma^+_g$	$\underline{-52.93}$ $1\,^1_3\Pi_u$	$\underline{-52.51}$ $1\,^1_3\Delta_g$	$\underline{-52.43}$ $1\,^1_3\Delta_u$	$\underline{-52.86}$ $1\,^1_3\Pi_g$	$\underline{-52.43}$ $1\,^1_3\Delta_u$
	$\underline{-52.51}$ $1\,^1_3\Delta_g$	$\underbrace{-51.66}$ $2\,^1_2\Pi_u$	-51.63 $2\,^1_4\Delta_g$	$\underline{-51.67}$ $1\,^1_3\Sigma^+_u$	$\underbrace{-52.24}$ $2\,^1_2\Pi_g$	
	-52.07 $1\,^3_4\Sigma^+_g$					
1	$\underline{-52.50}$ $1\,^3_3\Delta_g$	$\underline{-52.93}$ $1\,^3_3\Pi_u$	$\underline{-52.98}$ $\mathbf{X\,3^3_3\Sigma^-_g}$	$\underbrace{-52.60}$ $1\,^3_2\Sigma^+_u$	$\underline{-52.86}$ $1\,^3_3\Pi_g$	$\underline{-52.89}$ $1\,^3_3\Sigma^-_u$
	$\underline{-51.00}$ $2\,^3_3\Delta_g$	$\underbrace{-52.23}$ $2\,^3_2\Pi_u$	$\underline{-52.50}$ $1\,^3_3\Delta_g$	$\underline{-52.43}$ $1\,^3_3\Delta_u$	$\underbrace{-52.23}$ $2\,^3_2\Pi_g$	$\underline{-52.43}$ $1\,^3_3\Delta_u$
		$\underline{-51.91}$ $1\,^3_3\Phi_u$	-52.08 $1\,^3_4\Sigma^-_g$		$\underline{-51.81}$ $1\,^3_3\Phi_g$	$\underbrace{-51.64}$ $1\,^3_2\Sigma^-_u$
2	-51.60 $1\,^5_4\Delta_g$	$\underline{-51.89}$ $1\,^5_3\Phi_u$	-51.60 $1\,^5_4\Delta_g$	$\underbrace{-51.32}$ $1\,^5_2\Delta_u$	$\underbrace{-52.23}$ $1\,^5_2\Pi_g$	$\underline{-52.89}$ $1\,^5_3\Sigma^-_u$
	$\underline{-50.98}$ $2\,^5_3\Delta_g$				$\underline{-51.87}$ $1\,^5_3\Phi_g$	$\underbrace{-51.63}$ $2\,^5_2\Sigma^-_u$

Table 6: Energies (in cm,$^{-1}$ first entry) and average values $\langle L^2_\perp\rangle = \langle L^2_x + L^2_y\rangle$ (a.u., second entry) of FCI-NO states for $(^{3,4}He)_4$-$Cl_2(X)$ clusters. The FCI-NO states are classified according to the symmetry within the D_{2h} point group and the total spin quantum number, S. Underlined (underlined with braces) values are associated to states posing about one (two) helium atoms at the two Cl_2 ends. This table is an extended version of Table 1 from our previous letter [5].

S	$\langle A_g,\, B_{1g} \,\vert\, L^\pm \,\vert\, B_{2g}/B_{3g}\rangle$		$\langle B_{3u}/B_{2u} \,\vert\, L^\pm \,\vert\, B_{1u},\, A_u\rangle$	
	$^4He_2@Cl_2(X)$			
0	$\langle X\,1^1_2\Sigma^+_g \vert L^- \vert 1\,1^1_1\Pi_g\rangle$	0.021	$\langle 1\,1^1_2\Pi_u \vert L^+ \vert 1\,1^1_1\Sigma^+_u\rangle$	0.050
	$\langle 2\,1^1_1\Sigma^+_g \vert L^- \vert 1\,1^1_1\Pi_g\rangle$	-0.054	$\langle 2\,1^1_1\Pi_u \vert L^+ \vert 1\,1^1_1\Sigma^+_u\rangle$	-0.016
	$\langle 3\,1^1_2\Sigma^+_g \vert L^- \vert 1\,1^1_1\Pi_g\rangle$	-0.010	$\langle 1\,1^1_2\Pi_u \vert L^- \vert 1\,1^1_1\Delta_u\rangle$	-0.024
	$\langle 2\,1^1_2\Delta_g \vert L^+ \vert 1\,1^1_1\Pi_g\rangle$	0.045	$\langle 2\,1^1_1\Pi_u \vert L^- \vert 1\,1^1_1\Delta_u\rangle$	-0.035
	$\langle 1\,1^1_2\Delta_g \vert L^+ \vert 1\,1^1_1\Pi_g\rangle$	0.054	$\langle 1\,1^1_2\Phi_u \vert L^+ \vert 1\,1^1_1\Delta_u\rangle$	-0.038
	$\langle 1\,1^1_1\Phi_g \vert L^+ \vert 1\,1^1_1\Pi_g\rangle$	0.016		
	$^3He_2@Cl_2(X)$			
0	$\langle X\,1^1_2\Sigma^+_g \vert L^- \vert 1\,1^1_1\Pi_g\rangle$	-0.042	$\langle 1\,1^1_2\Pi_u \vert L^+ \vert 1\,1^1_1\Sigma^+_u\rangle$	-0.130
	$\langle 2\,1^1_1\Sigma^+_g \vert L^- \vert 1\,1^1_1\Pi_g\rangle$	0.001	$\langle 1\,1^1_2\Pi_u \vert L^- \vert 1\,1^1_1\Delta_u\rangle$	-0.055
	$\langle 1\,1^1_2\Delta_g \vert L^+ \vert 1\,1^1_1\Pi_g\rangle$	0.122		
1	$\langle 1\,1^3_1\Sigma^+_g \vert L^- \vert 1\,1^3_1\Pi_g\rangle$	0.015	$\langle 1\,1^3_2\Pi_u \vert L^+ \vert 1\,1^3_1\Sigma^+_u\rangle$	-0.139
	$\langle 1\,1^3_2\Sigma^-_g \vert L^- \vert 1\,1^3_1\Pi_g\rangle$	-0.149	$\langle 1\,1^3_2\Pi_u \vert L^- \vert 1\,1^3_1\Delta_u\rangle$	-0.010
			$\langle 2\,1^3_1\Pi_u \vert L^+ \vert 1\,1^3_1\Sigma^+_u\rangle$	-0.029
			$\langle 2\,1^3_1\Pi_u \vert L^- \vert 1\,1^3_1\Delta_u\rangle$	-0.006

Table 7: $\langle L^\pm\rangle$ coupling terms between FCI-NO states for $^4He_2@Cl_2(X)$ and $^3He_2@Cl_2(X)$.

S	$\langle A_g,\, B_{1g} \mid L^{\pm} \mid B_{2g}/B_{3g} \rangle$		$\langle B_{3u}/B_{2u} \mid L^{\pm} \mid B_{1u},\, A_u \rangle$	
	$^4He_3@Cl_2(X)$			
0	$\left\langle X\,{}^1_3\Sigma^+_g \right\vert L^- \left\vert 1\,{}^1_3\Pi_g \right\rangle$	0.032	$\langle 1\,{}^1_3\Phi_u \vert L^+ \vert 1\,{}^1_2\Sigma^+_u \rangle$	0.057
	$\left\langle 2\,{}^1_2\Sigma^+_g \right\vert L^- \left\vert 1\,{}^1_2\Pi_g \right\rangle$	0.008	$\langle 1\,{}^1_2\Pi_u \vert L^+ \vert 1\,{}^1_2\Sigma^+_u \rangle$	0.019
	$\langle 1\,{}^1_2\Delta_g \vert L^+ \vert 1\,{}^1_2\Pi_g \rangle$	−0.010	$\langle 2\,{}^1_3\Pi_u \vert L^+ \vert 1\,{}^1_2\Sigma^+_u \rangle$	−0.047
	$\left\langle 3\,{}^1_1\Sigma^+_g \right\vert L^- \left\vert 1\,{}^1_2\Pi_g \right\rangle$	0.047	$\langle 3\,{}^1_1\Pi_u \vert L^+ \vert 1\,{}^1_2\Sigma^+_u \rangle$	−0.017
	$\langle 1\,{}^1_2\Delta_g \vert L^- \vert 1\,{}^1_1\Phi_g \rangle$	0.046	$\langle 1\,{}^1_2\Pi_u \vert L^- \vert 1\,{}^1_2\Delta_u \rangle$	−0.005
	$\langle 1\,{}^1_2\Delta_g \vert L^+ \vert 1\,{}^1_2\Pi_g \rangle$	0.010	$\langle 2\,{}^1_3\Pi_u \vert L^- \vert 1\,{}^1_2\Delta_u \rangle$	0.012
	$\langle 2\,{}^1_3\Delta_g \vert L^+ \vert 1\,{}^1_2\Pi_g \rangle$	−0.042	$\langle 3\,{}^1_1\Pi_u \vert L^- \vert 1\,{}^1_2\Delta_u \rangle$	0.048
	$\langle 3\,{}^1_2\Delta_g \vert L^+ \vert 1\,{}^1_2\Pi_g \rangle$	0.019	$\langle 2\,{}^1_2\Phi_u \vert L^- \vert 1\,{}^1_2\Delta_u \rangle$	0.041
	$\langle 2\,{}^1_3\Delta_g \vert L^- \vert 1\,{}^1_1\Phi_g \rangle$	0.015	$\langle 1\,{}^1_2\Pi_u \vert L^+ \vert 2\,{}^1_2\Sigma^+_u \rangle$	−0.043
	$\langle 3\,{}^1_2\Delta_g \vert L^- \vert 1\,{}^1_1\Phi_g \rangle$	−0.001	$\langle 2\,{}^1_3\Pi_u \vert L^+ \vert 2\,{}^1_2\Sigma^+_u \rangle$	0.008
			$\langle 3\,{}^1_1\Pi_u \vert L^+ \vert 2\,{}^1_2\Sigma^+_u \rangle$	0.406
			$\langle 1\,{}^1_3\Phi_u \vert L^+ \vert 1\,{}^1_2\Delta_u \rangle$	−0.057
			$\langle 1\,{}^1_2\Pi_u \vert L^- \vert 1\,{}^1_2\Delta_u \rangle$	−0.006
			$\langle 2\,{}^1_3\Pi_u \vert L^- \vert 1\,{}^1_2\Delta_u \rangle$	0.012
			$\langle 3\,{}^1_1\Pi_u \vert L^- \vert 1\,{}^1_2\Delta_u \rangle$	0.048
			$\langle 2\,{}^1_2\Phi_u \vert L^+ \vert 1\,{}^1_2\Delta_u \rangle$	−0.033
			$\langle 1\,{}^1_3\Phi_u \vert L^+ \vert 2\,{}^1_2\Delta_u \rangle$	−0.007
			$\langle 1\,{}^1_2\Pi_u \vert L^- \vert 2\,{}^1_2\Delta_u \rangle$	0.037
			$\langle 2\,{}^1_3\Pi_u \vert L^- \vert 2\,{}^1_2\Delta_u \rangle$	−0.013
			$\langle 3\,{}^1_1\Pi_u \vert L^- \vert 2\,{}^1_2\Delta_u \rangle$	−0.013
			$\langle 2\,{}^1_1\Phi_u \vert L^+ \vert 2\,{}^1_2\Delta_u \rangle$	−0.005
	$^3He_3@Cl_2(X)$			
0	$\left\langle 1\,{}^1_2\Sigma^+_g \right\vert L^- \left\vert 1\,{}^2_2\Pi_g \right\rangle$	0.008	$\langle 1\,{}^2_3\Pi_u \vert L^+ \vert 1\,{}^2_2\Sigma^+_u \rangle$	0.123
	$\left\langle 1\,{}^1_2\Sigma^+_g \right\vert L^- \left\vert 2\,{}^2_2\Pi_g \right\rangle$	0.016	$\langle 1\,{}^2_3\Pi_u \vert L^+ \vert 2\,{}^2_1\Sigma^+_u \rangle$	0.011
	$\langle 1\,{}^2_3\Delta_g \vert L^+ \vert 1\,{}^2_2\Pi_g \rangle$	−0.093	$\langle 1\,{}^2_3\Pi_u \vert L^+ \vert 1\,{}^2_2\Sigma^-_u \rangle$	0.062
	$\langle 1\,{}^2_3\Delta_g \vert L^+ \vert 2\,{}^2_2\Pi_g \rangle$	0.057	$\langle 2\,{}^2_2\Pi_u \vert L^+ \vert 1\,{}^2_2\Sigma^+_u \rangle$	−0.016
	$\left\langle 1\,{}^2_2\Sigma^-_g \right\vert L^- \left\vert 1\,{}^2_2\Pi_g \right\rangle$	−0.036	$\langle 2\,{}^2_2\Pi_u \vert L^+ \vert 2\,{}^2_1\Sigma^+_u \rangle$	0.063
	$\left\langle 1\,{}^2_2\Sigma^-_g \right\vert L^- \left\vert 2\,{}^2_2\Pi_g \right\rangle$	0.022	$\langle 2\,{}^2_2\Pi_u \vert L^+ \vert 1\,{}^2_2\Sigma^-_u \rangle$	−0.092
1	$\langle 2\,{}^4_2\Delta_g \vert L^+ \vert 1\,{}^4_2\Pi_g \rangle$	−0.015	$\langle 1\,{}^4_2\Pi_u \vert L^- \vert 1\,{}^4_2\Delta_u \rangle$	−0.007
	$\langle 2\,{}^4_2\Delta_g \vert L^+ \vert 2\,{}^4_1\Pi_g \rangle$	−0.003	$\langle 1\,{}^4_2\Pi_u \vert L^+ \vert 1\,{}^4_2\Sigma^-_u \rangle$	−0.012
	$\left\langle X\,{}^4_3\Sigma^-_g \right\vert L^- \left\vert 1\,{}^4_2\Pi_g \right\rangle$	0.140	$\langle 1\,{}^4_3\Phi_u \vert L^+ \vert 1\,{}^4_2\Delta_u \rangle$	0.091
	$\left\langle X\,{}^4_3\Sigma^-_g \right\vert L^- \left\vert 2\,{}^4_1\Pi_g \right\rangle$	−0.004		
	$\left\langle 2\,{}^4_2\Sigma^-_g \right\vert L^- \left\vert 1\,{}^4_2\Pi_g \right\rangle$	−0.027		
	$\left\langle 2\,{}^4_2\Sigma^-_g \right\vert L^+ \left\vert 2\,{}^4_1\Pi_g \right\rangle$	0.139		

Table 8: $\langle L^{\pm} \rangle$ coupling terms between FCI-NO states for $^4He_2@Cl_3(X)$ and $^3He_3@Cl_2(X)$.